ENGINEERING Information Technology & Electronic Engineering
https://www.academax.com/EITEE; https://www.engineering.org.cn
https://ieeexplore.ieee.org/xpl/RecentIssue.jsp?punumber=11344065
E-mail: eng.itee@zju.edu.cn

Engineering Journals
Available on IEEE Xplore®

Research Article
https://doi.org/10.1631/ENG.ITEE.2025.0134

A polarization-switchable metasurface antenna for communication and meteorological radar systems

Qi ZOU[1], Fuwei LI[1,2✉], Pei XIAO[1], Qi LIU[3], Gaosheng LI[1]

[1]*College of Electrical and Information Engineering, Hunan University, Changsha 410082, China*
[2]*Changsha Institute of Mining Research Co., Ltd., Changsha 410012, China*
[3]*Xinjiang Astronomical Observatory, Chinese Academy of Sciences, Urumqi 830011, China*

Abstract: A highly integrated and compact dual circularly and linearly polarized metasurface antenna array operating in the X-band is developed in this study. By implementing an aperture-sharing configuration that enables two radiating patch elements to be shared between left- and right-hand circular polarization channels, significant miniaturization and efficient spatial utilization are achieved for multifunctional airborne meteorological radar and communication platforms. The introduction of a sequential-rotation feeding structure and metasurface patches enhances the circular polarization bandwidth characteristics of the antenna. Miniaturization of the dual circular polarization array and efficient spatial utilization are achieved by sharing two patch elements. Additionally, the simultaneous operation of the two circular polarization ports provides linear polarization radiation functionality. A microwave imaging example based on a back-projection algorithm is implemented to demonstrate the meteorological detection capability of the designed antenna. The antenna is simulated and physically designed, yielding a measured impedance bandwidth of 9.6–14 GHz (37.39%), a 3-dB gain bandwidth of 10.6–13.56 GHz (23.5%), and a peak gain of 12.83 dBi at 12 GHz. Stable dual circularly and linearly polarized radiation is exhibited, demonstrating versatile polarization-switchable characteristics that are ideal for airborne meteorological radar systems to detect weather conditions ahead of the aircraft and enable simultaneous communication capabilities.

Key words: Polarization-switchable antenna; Dual circular polarization (DCP); Metasurface; Meteorological radar

1 Introduction

Airborne meteorological radar antennas serve as the eyes of an aircraft to visualize the flight path and are critical for ensuring that the aircraft navigates safely and avoids extreme cloud weather (Weber et al., 2021; Notaroš, 2022). Compared to linearly polarized electromagnetic waves, circularly polarized ones offer numerous advantages, such as reducing the effects of multipath interference, enhancing anti-jamming capabilities, and minimizing polarization mismatches between transmission and reception (Xu et al., 2020). As a result, circularly polarized antennas are increasingly used in airborne meteorological radar technology. Moreover, owing to the growing need for multifunctional integration in radar and airborne communication, multi-polarization antennas have become an increasingly important research topic (Alaqeel et al., 2019; Mao et al., 2024).

Most meteorological radars employ linear polarization waves, whereas circular polarization is frequently used for detecting meteorological phenomena, such as hail, owing to its orthogonal electromagnetic wave reflection characteristics (Nekrasov and Dell'Acqua, 2016; Cao et al., 2017). When a radar transmits circularly polarized waves, spherical raindrops produce echoes in the orthogonal circular polarization state. In contrast, non-spherical particles (e.g., hail) induce depolarization effects on circularly polarized waves. By exploiting the depolarization characteristics of non-spherical hailstones in echo signatures, circularly polarized radars can effectively identify hail within storm systems (Al-Jumily et al., 1991). Consequently, research on multi-polarized, multichannel detection radars provides significant scientific and practical value (Yin et al., 2021; Li et al., 2025).

In recent years, the growing demand for dual circular polarization (DCP) has prompted increasingly diverse research (Banerjee et al., 2020; Schlaffer and Schlögl, 2024). Antennas based on Fabry–Perot resonant cavities use dual-port linear polarization feeding to achieve DCP radiation through a partially reflective surface (Zhao XQ et al., 2024). However, such cavities have relatively large profiles and dimensions. Dual-port crossed dipoles and magnetoelectric

✉ Fuwei LI, 18974939931@163.com
Qi ZOU, https://orcid.org/0000-0003-1623-7654
Pei XIAO, https://orcid.org/0000-0002-9214-8461
Gaosheng LI, https://orcid.org/0000-0001-5230-1428
CLC number: TN82

Received: Nov. 14, 2025; Revision accepted: July 13, 2026;
Crosschecked: Aug. 4, 2026

dipoles, designed for the L-band and C-band microwave frequencies, respectively, are commonly used to achieve high-performance DCP radiation (Chen et al., 2020; Govindarajan et al., 2020; Zhang L et al., 2024). However, their all-metal structures and large reflective ground planes hinder antenna integration and miniaturization.

Planar microstrip antennas are an important configuration in the field of circularly polarized antennas owing to their low profile and ease of fabrication (Hossen et al., 2024; Moharana and Dwivedy, 2024). Dual-port circular polarization is easily achieved using a 3-dB coupler (Ta et al., 2022), but array alignment introduces complexity in the feed network design. Antennas with a sequential feeding structure achieve improved circular polarization, but their gain and efficiency performance are not optimal (Shen et al., 2016). Additionally, metasurfaces based on characteristic mode analysis are often used to achieve circular polarization because of their simple structure (Liu et al., 2024).

Recently, integrated metasurface architectures have emerged as key enabling hardware for next-generation wireless infrastructure, such as holographic multiple-input multiple-output communications (Gong et al., 2024a, 2024b). These advanced paradigms require low-profile, multi-polarization agile apertures to increase the spatial degrees of freedom within a confined footprint. Consequently, the shared-aperture polarization-switchable metasurface design developed in this study holds great promise for high-precision radar surveillance and future holographic communication networks.

To address the strict space and aerodynamic constraints of modern airborne platforms, this study develops a compact, multifunctional aperture-sharing metasurface antenna. The proposed design achieves polarization switchability through a highly integrated hardware architecture that combines a sequentially rotated feeding network with a shared-element metasurface superstrate. The core contribution of this study is the efficient implementation of wideband, multi-polarization capabilities within a highly confined physical volume, making it highly suitable for multifunctional airborne meteorological radar (AMR) and communication front-ends. As depicted in Fig. 1, the polarization-switchable antenna design leverages the scattering characteristics of electromagnetic waves for airborne weather radar applications, enabling the detection of storm cells ahead of the aircraft. The antenna's operational modes, including left-hand circular polarization (LHCP), right-hand circular polarization (RHCP), and linear polarization (LP), facilitate the multi-dimensional sensing of meteorological environments and enable simultaneous communication capabilities. This advanced, diverse polarization capability significantly enhances the acquisition of comprehensive and precise meteorological information.

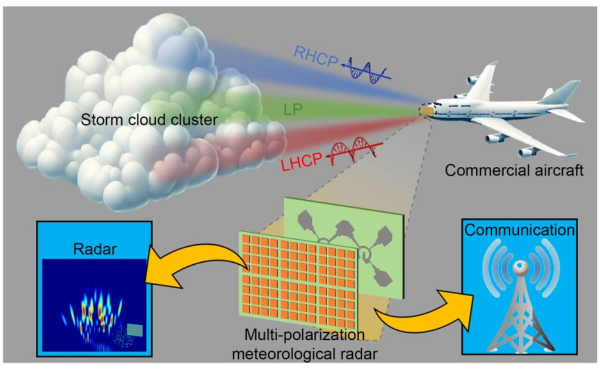

Fig. 1 Diagram of a polarization-switchable airborne radar

2 Polarization-switchable antenna design

2.1 Antenna geometry

The configuration of the proposed antenna array is shown in Fig. 2, which consists of a sequential-rotation feeding array sharing two elements and a rectangular patch array of metamaterials. The sequential-rotation feeding array comprises four corner-cut patches, impedance matching stubs, and quarter-wavelength phase-power matching lines. A 4×4 metasurface sub-array is placed above each corner-cut rectangular patch. The upper metasurface dielectric substrate and lower sequential-rotation feeding array dielectric substrate are made of F4B35 material (with a relative permittivity of 3.5 and a dielectric loss tangent of 0.001), with thicknesses of 1 mm and 0.5 mm, respectively. Two-direction sequential-rotation feeding arrays sharing two radiating element patches enable the radiation of directional DCP beams. The upper rectangular patch metasurface array is excited to generate circularly polarized resonant currents to produce secondary radiation, thereby improving the bandwidth, gain, and other characteristics of the circularly polarized beam.

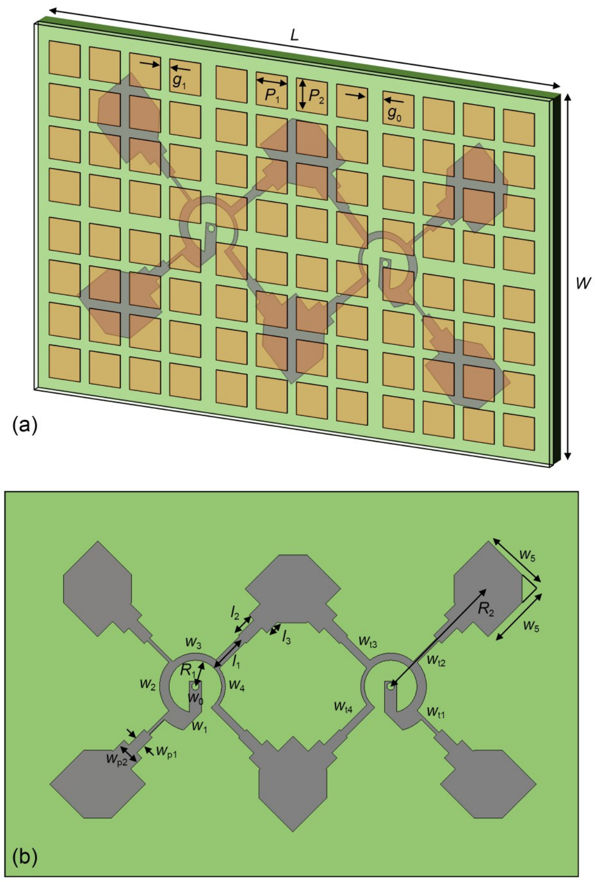

Fig. 2 Geometry of the proposed antenna array: (a) 3D view; (b) top view of the sequential-rotation feeding array. L=70 mm, W=50 mm, P_1=4.1 mm, P_2=3.8 mm, g_0=1 mm, g_1=0.55 mm, w_0=1.1 mm, w_1=1.74 mm, w_2=0.88 mm, w_3=0.66 mm, w_4=0.35 mm, w_5=0.35 mm, w_{t1}=0.3 mm, w_{t2}=0.32 mm, w_{t3}=0.69 mm, w_{t4}=0.74 mm, w_{p1}=1.04 mm, w_{p2}=2.3 mm, R_1=2.4 mm, R_2=12.65 mm, l_1=3.7 mm, l_2=1.99 mm, and l_3=1.46 mm

2.2 Analysis of circularly polarized radiation

The sequential-rotation feeding array structure achieves a 90° phase delay and power distribution through arc-shaped stubs (Sun et al., 2020). Consequently, the arc length between each patch element is approximately a quarter wavelength. The width of each arc is calculated based on the circuit model shown in Fig. 3. The green transmission lines represent the arc phase line in the sequential-rotation feeding array structure, which provides the required 90° phase shift. The blue transmission lines are quarter-wavelength impedance Transformers, ensuring that the impedance at each node (such as nodes A and B) is matched to a 50-Ω antenna port. Because the four antennas are fed in series, the power distribution ratio at each node must be considered to determine the impedance values for each branch of the network. The impedance of each transmission line is calculated using Eq. (1):

$$\begin{cases} Z_{n1}=\dfrac{Z_{\mathrm{T}n}^2}{Z_0},\ Z_{n2}=Z_n, \\ \dfrac{Z_{n1}}{Z_{n2}}=k_n,\ Z_{A1}\|Z_{A2}=Z_0,\ n=A, B, C, D, \end{cases} \tag{1}$$

where Z_0 is the input impedance of the coaxial line and is set to 50 Ω, and k_n represents the impedance ratio of the power-flow path at node n, and Z_{n1} and Z_{n2} denote the input impedances looking into the antenna branch and the subsequent path at node n, respectively. In addition, $Z_{\mathrm{T}n}$ denotes the impedance of the impedance Transformer in the corresponding branch of node n, while Z_n represents the equivalent impedance looking from node n toward the subsequent path.

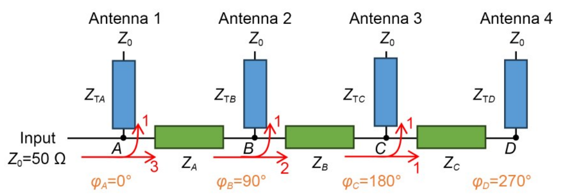

Fig. 3 Circuit model of the sequential-rotation feeding array

Through analysis and design of the above circuit model, signals with equal amplitudes and 90° phase differences relative to the signals fed into the four corner-cut patches are achieved. Additionally, the antenna elements are rotated according to phase variations, resulting in improved circular polarization radiation characteristics. Furthermore, to extend the circular-polarization impedance and axial ratio (AR) bandwidth, small rectangular metallic metasurface structures are placed above each patch element. The gaps within the metallic structures are excited to improve the high-frequency performance, further enhancing the efficient radiation of the circularly polarized electromagnetic waves.

The sequential-rotation feeding array network uses circularly polarized signals as the excitation source, which maintains equal amplitudes with a 90° phase difference, enabling effective excitation of the metasurface unit cell using a simple, small, square metallic patch. This configuration generates two orthogonal currents with equal amplitudes and a 90° phase difference, thereby realizing circularly polarized radiation (Deng et al., 2023). Furthermore, each 4×4 sub-metasurface region corresponds to a sub-feed element in the sequential-rotation feeding array, whereas each 2×2 sub-metasurface region is associated with a specific circularly polarized excitation. This innovative configuration enables a sharing mechanism between two sub-metasurface regions, resulting in a significant reduction in the aperture size of the antenna.

To better analyze the excitation mechanism of circularly polarized radiation in metasurfaces, the characteristic mode theory has been employed for antenna analysis (Zhao C and Wang, 2018; Sharif et al., 2023; Wang et al., 2024). This theoretical approach provides valuable insights into the modal behavior and radiation characteristics of metasurface-based antenna structures. The total excitation current on a perfectly electrically conducting object is decomposed into a vector superposition of individual modal currents (Liu et al., 2024). To better analyze the excitation mechanism of circularly polarized radiation in metasurfaces, the characteristic mode theory has been employed for antenna analysis (Zhao C and Wang, 2018; Sharif et al., 2023; Wang et al., 2024).

Through a comprehensive analysis of the modal weighting coefficients and phase characteristics associated with each mode, we effectively predict and evaluate the radiation characteristics of the proposed structure. This analytical approach provides a systematic methodology for understanding the electromagnetic behavior and optimizing the radiation performance of the antenna system.

$$\boldsymbol{J}=\sum\nolimits_{n=1}^{N} c_n \boldsymbol{J}_n. \tag{2}$$

Eq. (2) shows that the total current is formed by the superposition of the current vector of each mode, where $\boldsymbol{J}_n$ represents the excitation current of mode n, and c_n represents its corresponding weighting coefficient. For simplicity, the characteristic modes of a single 4×4 sub-metasurface region are analyzed independently. The corresponding modal weighting coefficients and phase distributions are presented in Fig. 4. Modes 1 and 2 exhibit identical weighting coefficients and phase characteristics, indicating the presence of a pair of degenerate modes. In contrast, modes 3 and 4 show a smaller weighting coefficient than modes 1 and 2. To further investigate the modal characteristics of the metasurface, the corresponding calculated modal current and far-field patterns are shown in Fig. 5.

Based on the modal current and far-field radiation patterns, modes 1 and 2 exhibit strongly consistent directional modal currents, enabling the generation of a robust main radiation beam. In

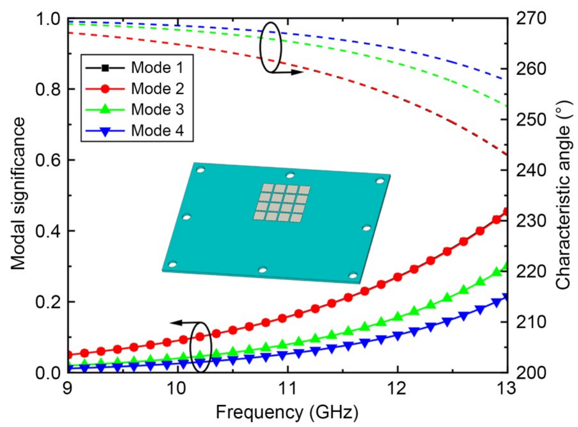

Fig. 4 Results of the characteristic mode analysis of the metasurface

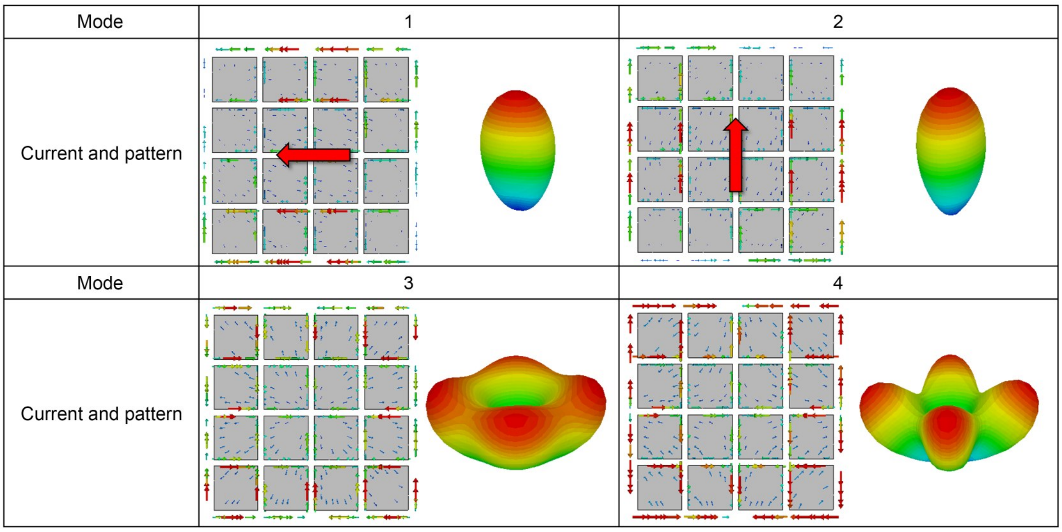

Fig. 5 Modal current distributions and far-field radiation patterns of four modes at 12 GHz

contrast, modes 3 and 4 produce loop currents at the corners, canceling the main radiation beam and forming four sidelobes. Owing to the concentrated, orthogonal orientation of the modal currents in modes 1 and 2, they can be easily excited by the underlying circularly polarized feed, thereby achieving circularly polarized radiation. Furthermore, according to the modal weighting coefficients, the circular-polarization excitation performance improves at higher frequencies. However, owing to feed-bandwidth limitations, the metasurface antenna demonstrates enhanced circular polarization performance at approximately 12 GHz.

2.3 Analysis of polarization switchability

The antenna design efficiently radiates three types of polarized electromagnetic waves and exhibits polarization-switchable characteristics with dual circularly and linearly polarized radiation. The left- and right-hand sequential-rotation feeding array networks enable the radiation of two types of circularly polarized electromagnetic waves. Owing to the strong isolation characteristic of the impedance of the sequential-rotation feeding array networks, the two corner-cut patch elements enable aperture sharing in the DCP antenna.

As shown in Fig. 6a, the current distribution at 11 GHz indicates that the radiating resonant currents are primarily concentrated in the left sequential-rotation feeding array structure, whereas the right metallic patch generates minimal resonant currents. Additionally, the region near the input port on the right-hand side exhibits lower currents, demonstrating that the structure has excellent port isolation. This is further confirmed by the isolation levels at most frequency points being below −15 dB (Fig. 6b). Notably, due to the complete structural symmetry, the isolation curves of the two ports are identical. The designed polarization aperture-sharing structure achieves excellent DCP characteristics and polarization isolation while achieving a compact antenna size.

Based on the principle of electromagnetic wave polarization, a linearly polarized wave can be decomposed into two circularly polarized waves, and vice versa. Assuming that the electromagnetic wave propagates outward along the plane, the electric field vectors of left- and right-hand circularly polarized electromagnetic waves are shown in Fig. 7.

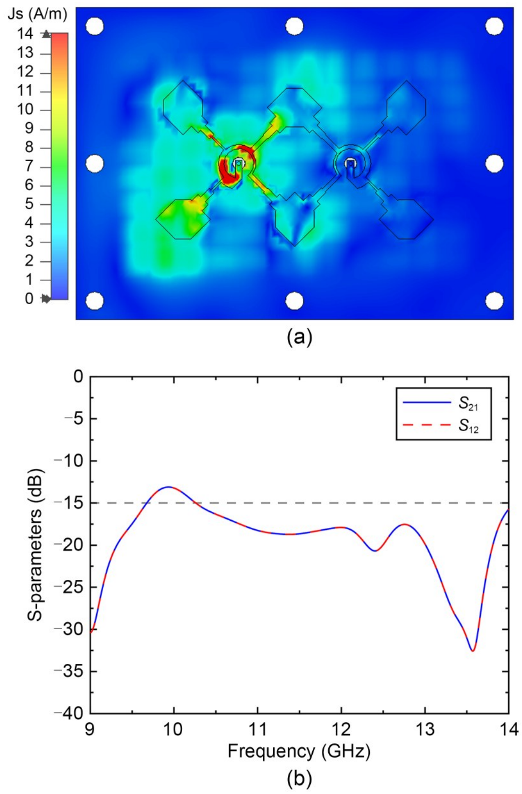

Fig. 6 Current distributions of the left-hand circularly polarized electromagnetic radiation at 11 GHz (a) and polarization isolation (b)

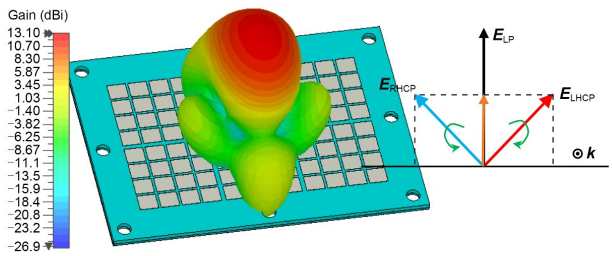

Fig. 7 Linear polarization radiation pattern and synthesis mechanism of the proposed antenna. *E* represents the electromagnetic field and *k* represents the propagation direction

If the amplitudes and phases of two circularly polarized electromagnetic waves are aligned, as shown in Fig. 7, at any given moment, the horizontal components of the two circularly polarized waves cancel, whereas their vertical components add. This results in a vertically and linearly polarized electromagnetic wave. Therefore, by simultaneously exciting the two ports of the designed antenna with amplitude- and phase-matched signals, linearly polarized electromagnetic radiation is generated.

3 Antenna results and discussions

3.1 Measurement configuration

To validate the polarization-switchable radiation capability of the designed antenna, the radiation characteristics of the fabricated antenna array are measured in an anechoic chamber. Fig. 8 shows the photographs of the fabricated prototype and the measurement setup in the microwave anechoic chamber. The antenna prototype consists of two stacked dielectric substrates fixed using nylon studs at the edges. The 50-Ω subminiature version A (SMA) connectors are soldered to each sequential-rotation feeding input port.

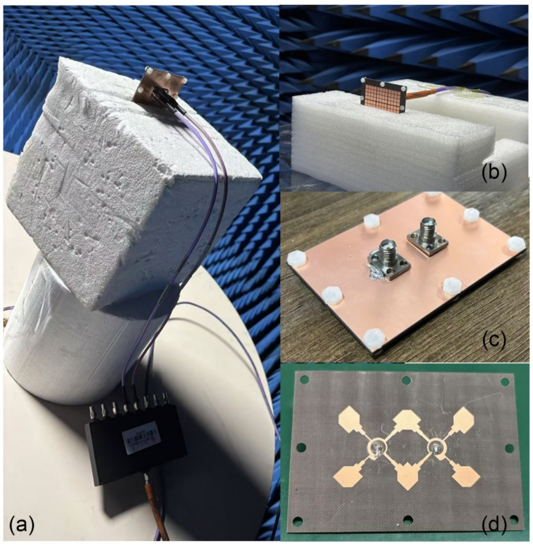

Fig. 8 Measurements of the LP (a) and CP (b) radiation patterns and the photographs of the fabricated antenna from back view (c) and front view (d). CP: circular polarization

The antenna radiation performance is tested using an E5063A vector network analyzer (VNA), as shown in Fig. 9. The two ports of the VNA are connected to a standard-gain transmitting horn antenna and the antenna under test (AUT) via low-noise amplifiers, separately. The AUT is mounted on a rotating platform to measure its radiation pattern. The entire radiation test setup is placed inside an anechoic chamber, where microwave-absorbing materials simulate ideal reflection-free conditions (Lee et al., 2025).

3.2 Measurement results

The simulated and measured S-parameter curves are shown in Fig. 10. The measured data are obtained using an E5063A VNA. The measured −10 dB impedance bandwidth of the CP mode is

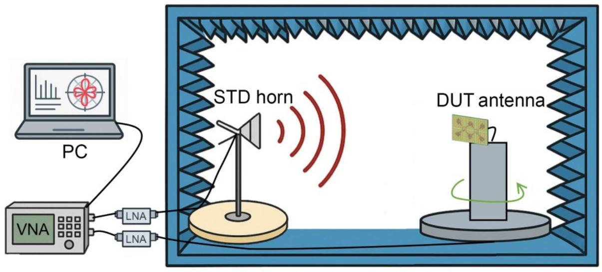

Fig. 9 Antenna measurements in the anechoic chamber. PC: personal computer; DUT: device under test; STD horn: standard horn antenna; LNA: low-noise amplifier

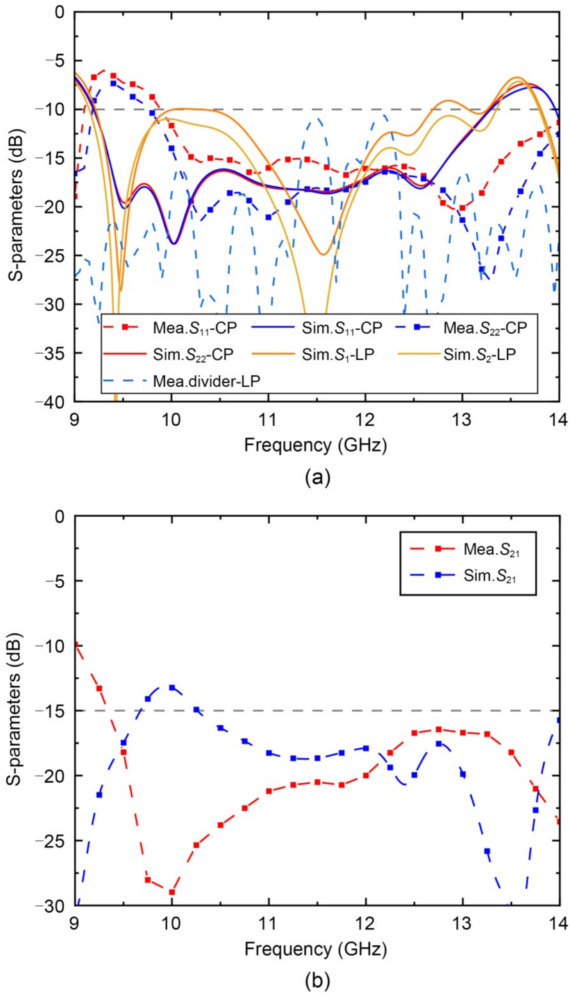

Fig. 10 Simulated and measured S-parameters of the designed antenna: (a) reflection coefficient; (b) port isolation

37.39% (9.6–14 GHz). Impedance matching under the LP operation is verified by evaluating the simulated active return loss (Sim.S_1-LP and Sim.S_2-LP) and the measured return loss using an external power divider (Mea.divider-LP). All curves remain well below −10 dB across the operational bandwidth, confirming stable dual-port impedance matching and robust hardware reliability. Additionally, the measured port isolation results closely match the simulation ones, with both achieving values below −15 dB.

To investigate the minor frequency shift between the simulated and measured results, a numerical tolerance study is performed.

As shown in Fig. 11, parametric sweeps demonstrate that the standard commercial tolerances in the substrate dielectric constant ($\varepsilon_r\pm0.1$) and thickness variations alter the electrical length of the metasurface elements, resulting in resonant deviations. Other practical assembly factors that are difficult to model precisely, such as parasitic effects from manual SMA soldering and variations in the microscopic gaps between layers induced by nylon screw fastening, contribute to the cumulative frequency shift. These simulated trends confirm that the experimental discrepancy is within reasonable fabrication and engineering margins.

Fig. 12 shows the gain and AR characteristics, whereas Fig. 13 shows the radiation pattern characteristics of the developed antenna tested in a microwave anechoic chamber. The simulated results indicate that the antenna achieves a maximum gain of 13.17 dBi at 11.1 GHz, with a 3-dB gain bandwidth (9.69–12.72 GHz) corresponding to a relative bandwidth of 27.04%. Additionally, the simulated 3-dB AR bandwidth range is 9.66–12.24 GHz, corresponding to a relative bandwidth of 22.1%.

Similarly, the measured radiation performance exhibits a frequency shift toward higher frequencies, consistent with the matching characteristics described earlier. This may be due to the compression of the two dielectric substrates, resulting in a reduced antenna thickness. The measured and simulated results exhibit similar trends, with an overall rightward shift of the measured curve. The measured antenna achieves a maximum gain of 12.83 dBi at 12 GHz, with a 3-dB relative bandwidth of 23.5% (10.6–13.56 GHz). Additionally, its measured 3-dB AR bandwidth is 10.6–13.2 GHz, corresponding to a relative bandwidth of 21.7%. Notably, the gain curve for linear polarization closely matches that of circular polarization.

Owing to the frequency shift in the measured results, comparing the radiation pattern characteristics at the same frequency points is not meaningful. Therefore, Fig. 13 presents the radiation patterns at the selected central frequency points for simulated and measured data. Fig. 13 shows the simulated radiation patterns for DCP and linear polarization at 11 GHz on the left and the measured radiation patterns at 12 GHz on the right. Owing to the symmetry of the DCP structure, the measured and simulated results indicate the symmetry of the circularly polarized radiation pattern and the characteristics of the sidelobe direction. The linearly polarized radiation pattern has a narrower beamwidth than the circularly polarized pattern. The measured beam is slightly wider than the simulated one, possibly due to the amplitude and phase errors introduced by the external power divider.

Notably, the antenna exhibits excellent cross-polarization isolation of the circularly polarized beam, with a maximum cross-polarization level of −11.6 dB. In contrast, the linearly polarized radiation pattern shows slight cross-polarization, with a maximum of −6.68 dB. Fortunately, owing to the fundamental principle of

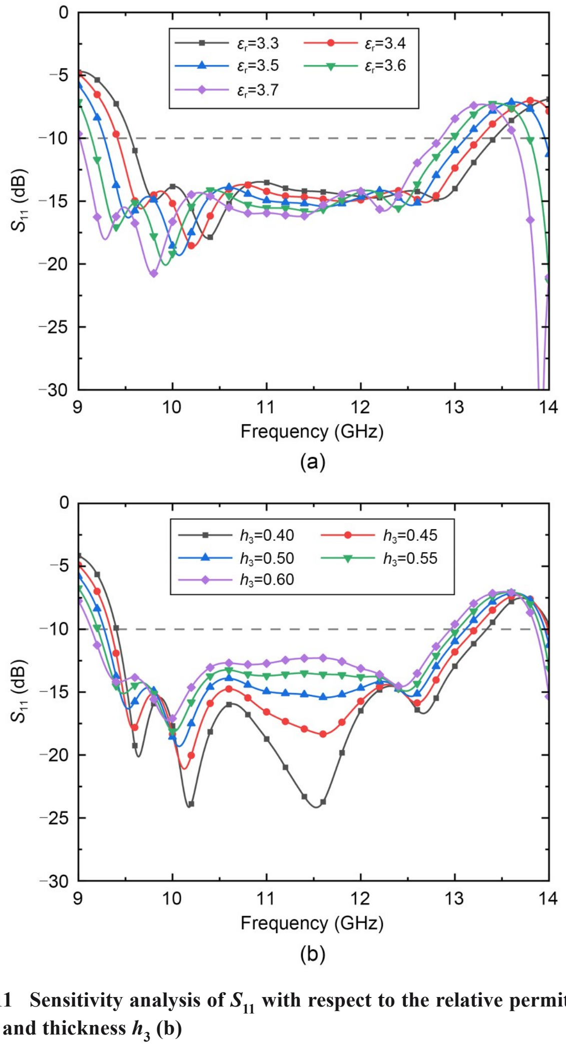

Fig. 11 Sensitivity analysis of S_{11} with respect to the relative permittivity ε_r (a) and thickness h_3 (b)

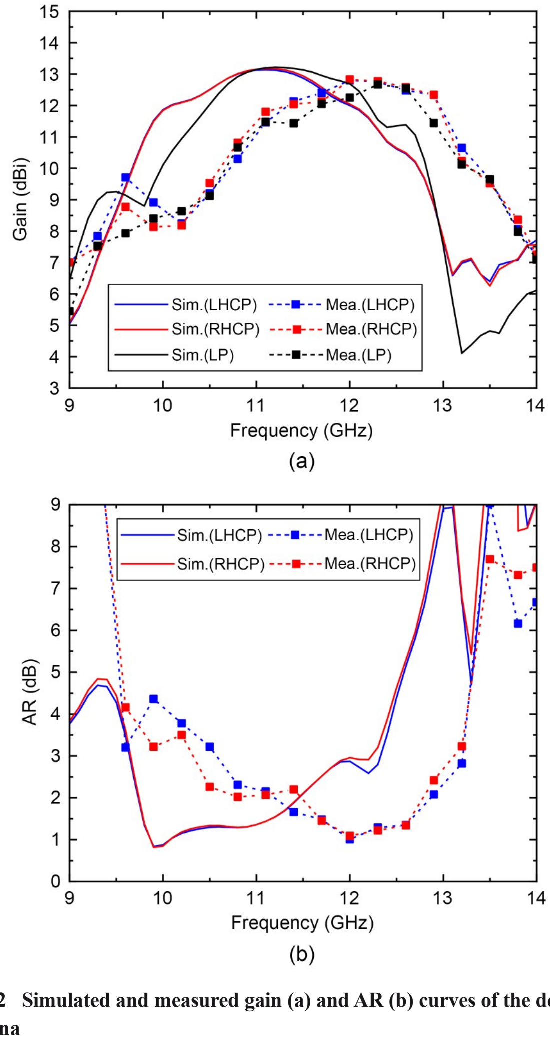

Fig. 12 Simulated and measured gain (a) and AR (b) curves of the designed antenna

circular polarization generation, the cross-polarization components of the two circular polarizations in the main radiation direction are opposite. When their vectors combine, they almost cancel, resulting in a very low cross-polarization level in the main radiation direction, which significantly reduces the impact of cross-polarization.

Notably, the synthesized LP radiation pattern exhibits a maximum cross-polarization level of −6.68 dB. This localized peak occurs exclusively at large oblique angles due to wide-angle edge scattering on the finite shared aperture. Cross-polarization suppression is lower than −25 dB within the primary main beam. From a system-level perspective, this wide-angle characteristic does not affect core meteorological classification because the discrimination of heavy precipitation and hail is performed predominantly via the high-purity DCP mode. For auxiliary target identification conducted in the LP state, any off-axis clutter leakage stemming from wide-angle cross-polarization can be mitigated in the radar backend signal processor using standard Doppler filtering and range-gating algorithms.

To demonstrate the advantages of the developed antenna, a comparison with relevant works is presented in Table 1. Compared to the reference antennas, the designed antenna achieves superior polarization-switchable performance within a more compact size, making it highly promising for X-band AMR.

To further clarify the explicit engineering merits of the proposed design for AMR applications, the critical trade-offs between profile, bandwidth, gain, and polarization flexibility highlighted in Table 1 need a deeper discussion. Standard AMR antennas that satisfy high gain and wideband multi-polarization requirements are generally bulky. In this work, the introduced metasurface layer overcomes

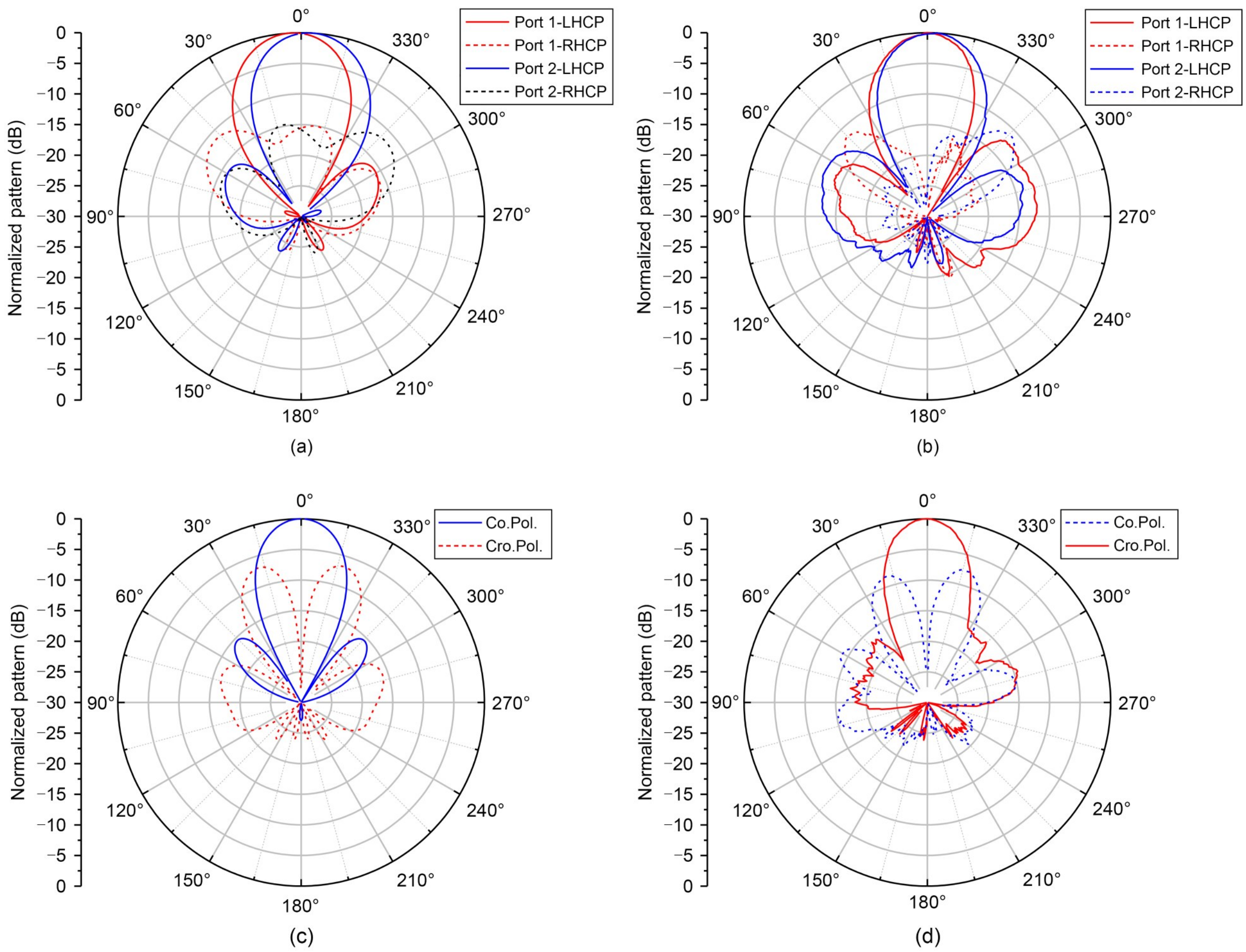

Fig. 13 Radiation patterns of the developed antenna: (a) simulated CPD pattern at 11 GHz; (b) measured CPD pattern at 12 GHz; (c) simulated LP pattern at 11 GHz; (d) measured LP pattern at 12 GHz. Co.Pol.: co-polarization; Cro.Pol.: cross-polarization

Table 1 Comparison of the developed antenna with others

Reference	Polarization	Center frequency (GHz)	Size	IBW (%)	3-dB gain BW (%)	Peak gain (dBi)
This work	DCP/LP	11	$2.570\lambda_0\times1.830\lambda_0\times0.055\lambda_0$	37.39	23.5	12.83
Zhao XQ et al., 2024	DCP	5.5	$2.860\lambda_0\times2.860\lambda_0\times0.580\lambda_0$	10.95	9.75	14.3
Ta et al., 2022	DCP	5.5	$0.770\lambda_0\times0.560\lambda_0\times0.070\lambda_0$	29.1	28.6	7.3
Shen et al., 2016	DCP	5.5	$3.594\lambda_0\times1.700\lambda_0\times0.059\lambda_0$	12.5	12.5	10.3
Reddy and Sheela, 2023	DCP	8.5	$2.850\lambda_0\times2.850\lambda_0\times0.059\lambda_0$	18	17.1	16.3

λ_0 is the wavelength of the center frequency. IBW: impedance bandwidth; BW: bandwidth these conventional limitations by facilitating a low-profile configuration without sacrificing radiation performance. Specifically, the re-resonant characteristic of the metasurface compensates for the bandwidth reduction typically caused by aperture miniaturization, yielding a high peak gain of 12.83 dBi to ensure long-range meteorological echo detection. Furthermore, through the dual-port aperture-sharing feeding topology, the antenna delivers full polarization flexibility (LHCP, RHCP, and synthesized LP) within a single compact physical footprint, avoiding the severe spatial and weight penalties of separate standalone arrays. Consequently, the optimized multidimensional architecture is highly suitable for space-constrained and aerodynamically strict airborne radar platforms.

4 Weather radar analysis

4.1 Characteristic analysis

For meteorological radar imaging analysis, it is necessary to introduce the electromagnetic characteristics of hail and raindrops as fundamental meteorological elements. Hail is considered as ice containing certain impurities, whereas raindrops are approximated as water. Therefore, the electrical properties of ice and water are used to approximate the electromagnetic characteristics of hail and raindrops, facilitating the construction of electromagnetic models. The more ordered molecular structure of ice than liquid water restricts the free movement of polar water molecules in the solid state, resulting in lower polarization capability and conductivity in ice than in water. Dry hail has a relative dielectric constant of 3.2 and electrical conductivity of 0.17 S/m, with a typical equivalent diameter ranging from 0.5 to 6 mm. In contrast, raindrops feature a much higher relative dielectric constant of 80 and an electrical conductivity of 0.01 S/m; their equivalent diameters generally fall within 0.5 to 5 mm (Shokr, 1998; Xie et al., 2022, 2024).

4.2 Imaging methodology

To demonstrate the potential of the developed antenna for AMR applications, we employ a simple back-projection imaging algorithm to simulate imaging, as shown in Fig. 14. This approach can somewhat verify the detection capability of our antenna design. The back-projection algorithm uses transmit–receive data (S_{21} parameter) from the antenna at different positions and frequencies to perform reverse tracing for each imaging point (Shi et al., 2022; Ogawa et al., 2024; Zhang JJ et al., 2024), followed by coherent superposition. Regions with strong scattering yield higher values after coherent superposition, whereas areas without scattering produce lower values, thereby enabling basic imaging of scattering objects.

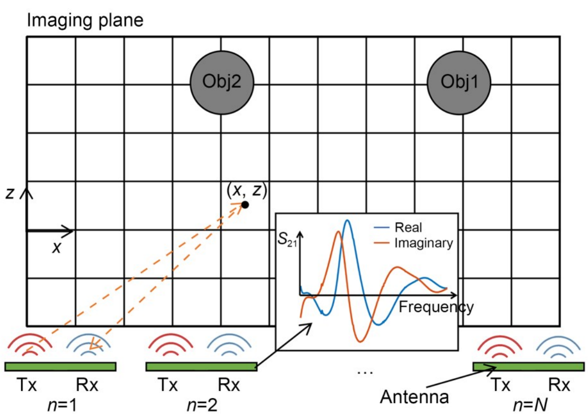

Fig. 14 Schematic of the back-projection algorithm detection. Tx: transmitting antenna; Rx: receiving antenna

$$I(x,z)=\sum_{n=1}^{N}\sum_{f=f_{\mathrm{L}}}^{f_{\mathrm{H}}} S_{21}(f,n)\,\mathrm{e}^{\mathrm{j}kr_n(x,z)}, \tag{3}$$

$$r_n(x,z)=\sqrt{(x-x_{rn})^2+z^2}+\sqrt{(x-x_{tn})^2+z^2}, \tag{4}$$

where f_{H} and f_{L} are the highest and lowest frequencies, respectively, and N is the total number of scanning points. $I(x, z)$ is the imaging intensity at point (x, z), and $S_{21}(f, n)$ is the S-parameter of the receiving and transmitting antennas at frequency f and position n. The propagation constant is given by $k=2\pi f/c$, and $r_n(x, z)$ is the electromagnetic wave propagation distance, i.e., the distance from the transceiver antenna to the imaging point (x, z). The coordinates of the transmitting and receiving antennas of the n^{th} scanning point are $(x_{tn}, 0)$ and $(x_{rn}, 0)$, respectively.

By leveraging the scattered S-parameter data acquired at different positions and frequencies, various imaging algorithms can be employed to reconstruct the image information of scattering objects. To validate the accuracy of the back-projection algorithm and facilitate subsequent differentiation between hail and raindrops, we perform microwave imaging of two metal spheres located at distinct (x, z) positions. Using 3D full-wave electromagnetic simulation software computer simulation technology (CST), we acquire the S-parameters between transmitting and receiving antennas across the 9–13 GHz frequency band at various scanning line positions. The data are post-processed using Eqs. (3) and (4), yielding microwave imaging results of the metal spheres shown in Fig. 15. Since the two metal spheres have identical material properties and dimensions, they produce two highly focused points with similar intensity and size at their respective locations, clearly indicating the presence of both spheres.

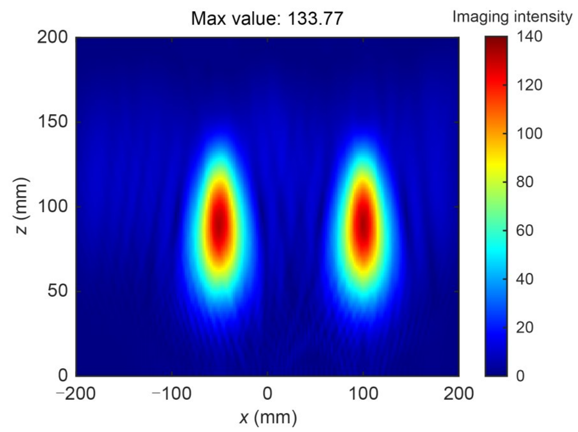

Fig. 15 Microwave imaging of two metal spheres

4.3 Simulations of radar imaging

To preliminarily evaluate the detection performance of the designed polarization-switchable antenna, we establish a simplified radar detection electromagnetic simulation model. This approach partially demonstrates the antenna's detection capabilities. Based on the previously described electromagnetic characteristics of hail and raindrops, we construct corresponding electromagnetic models in the 3D full-wave electromagnetic simulation software. These models include hail and raindrop clusters with a radius of 40 mm. The DCP antenna is then employed for microwave image detection to identify and differentiate the specific meteorological targets.

The microwave imaging results of hail and raindrop clusters in Fig. 16 are obtained by processing the S_{21} echo parameters acquired with the developed DCP antenna. The raindrop clusters exhibit significantly stronger intensity in the imaging distribution due to their higher dielectric constant and conductivity, generating more intense reflected signals than the hail clusters. Moreover, owing to the significant differences in shape between hail and raindrop clusters, their respective microwave images exhibit distinct characteristics, enabling further discrimination based on morphological features. Note that the actual meteorological radar detection is far more complex than this simplified process. The microwave imaging example presented above serves only to verify that our polarization-switchable antenna exhibits sufficiently robust meteorological detection performance.

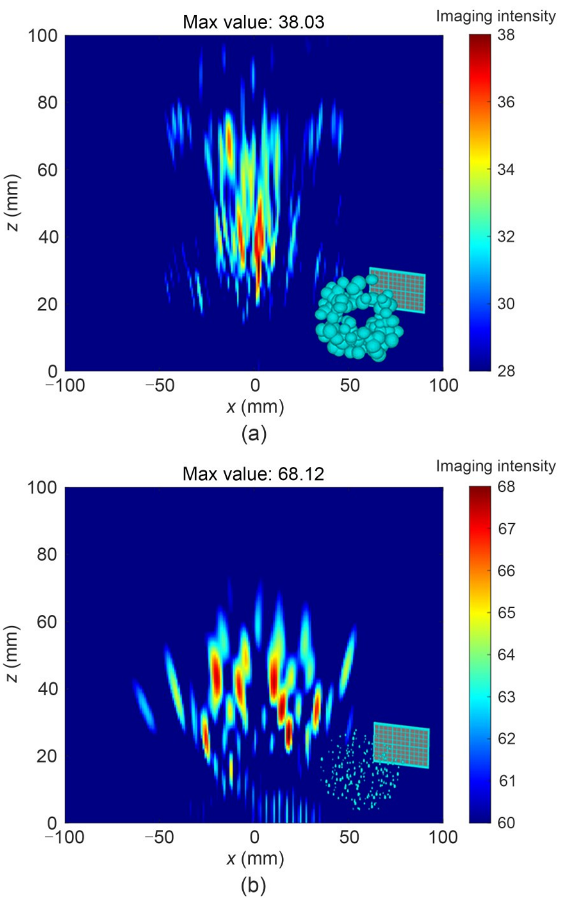

Fig. 16 Microwave imaging of hail (a) and raindrop (b) clusters

4.4 Quantitative link to radar system-level performance

Advanced polarimetric radar classification relies heavily on the precision of the circular depolarization ratio (CDR) (Cao et al., 2017) to identify highly nonspherical or tumbling hydrometeors, such as hail. The system-level CDR estimation accuracy is fundamentally restricted by the antenna's intrinsic cross-polarization isolation (CPI). The measured radiation patterns in Fig. 13 show that the proposed metasurface antenna exhibits a maximum CPI exceeding 25 dB in the broadside direction (θ=0°). Considering the entire angular range, the measured minimum CPI is 11.6–12 GHz. This high polarization purity guarantees that antenna-induced polarization crosstalk remains negligible around the core radiation zone. Consequently, the captured cross-polarization echo power is overwhelmingly dominated by the physical geometric asymmetry of weather targets rather than by hardware limitations.

The polarization suppression levels illustrated in Fig. 10b, governed by the isolation of the circular-polarization ports, directly determine the radar's clutter rejection ratio against volume rain clutter (Notaroš, 2022). As shown in Fig. 10b, the measured port isolation (S_{21}) is at least 16 dB across the 9–14 GHz band, with typical values below 15 dB, which translates into a co-to-cross polarization ratio exceeding 15 dB. Owing to the handedness reversal of circularly polarized waves upon reflection from symmetric targets, spherical raindrops convert an incident LHCP wave into an RHCP return signal. The high port isolation enables a rain clutter mitigation capability of 15–20 dB within the primary radar illumination sector. Concurrently, by switching the system feed to synthesize the linear polarization state, the radar can acquire multi-polarimetric data blocks. This facilitates advanced space-time adaptive processing or Doppler filtering to effectively suppress stationary surface clutter while preserving low-amplitude weather echo returns.

5 Conclusions

A compact, low-profile, and multifunctional metasurface antenna implementation was developed for X-band AMR applications. By strategically employing an aperture-sharing feeding topology and a shared re-resonant metasurface layer, the antenna successfully delivered LHCP, RHCP, and synthesized LP radiation without expanding the overall aperture dimensions. Validation experiments confirmed that this highly integrated implementation balances the crucial trade-off between wideband performance, polarization versatility, and strict compact-size requirements of modern radar and communication sharing.

Acknowledgments

This work was supported by the State Key Laboratory Special Programs of China Minmetals Corporation (No. 2024GZKJ02).

Author contributions

Qi ZOU designed the research and processed the data. Qi ZOU, Qi LIU, and Pei XIAO drafted the paper. Fuwei LI and Gaosheng LI helped organize the paper. Qi ZOU revised and finalized the paper.

Conflict of interest

All the authors declare that they have no conflict of interest.

Data availability

The data that support the findings of this study are available from the corresponding author upon reasonable request.

Declaration on the use of generative AI tools

During the preparation of this work, the authors used ChatGPT to improve language. After using this tool, the authors reviewed and edited the content as needed and take full responsibility for the content of the published article.

References

Alaqeel AA, Ibrahim AA, Nashashibi AY, et al., 2019. Experimental characterization of multi-polarization radar backscatter response of vehicles at J-band. *IEEE Trans Intell Transp Syst*, 20(9):3337-3350. https://doi.org/10.1109/TITS.2018.2876155

Al-Jumily KJ, Charltona RB, Humphries RG, 1991. Identification of rain and hail with circular polarization radar. *J Appl Meteor Climatol*, 30(8):1075-1087. https://doi.org/10.1175/1520-0450(1991)030<1075:IORAHW>2.0.CO;2

Banerjee U, Karmakar A, Saha A, 2020. A review on circularly polarized antennas, trends and advances. *Int J Microw Wirel Technol*, 12(9):922-943. https://doi.org/10.1017/S1759078720000331

Cao Q, Knight M, Ryzhkov AV, et al., 2017. Differential phase calibration of linearly polarized weather radars with simultaneous transmission/reception for estimation of circular depolarization ratio. *IEEE Trans Geosci Remote Sens*, 55(1):491-501. https://doi.org/10.1109/TGRS.2016.2609421

Chen WH, Yu ZQ, Zhai JF, et al., 2020. Developing wideband dual-circularly polarized antenna with simple feeds using magnetoelectric dipoles. *IEEE Antenn Wirel Propag Lett*, 19(6):1037-1041. https://doi.org/10.1109/LAWP.2020.2988560

Deng JH, Xiong H, Yang Q, et al., 2023. Metasurface-based microwave power detector for polarization angle detection. *IEEE Sens J*, 23(19):22459-22465. https://doi.org/10.1109/JSEN.2023.3306462

Gong TR, Wei L, Huang CW, et al., 2024a. Holographic MIMO communications with arbitrary surface placements: near-field LoS channel model and capacity limit. *IEEE J Sel Areas Commun*, 42(6):1549-1566. https://doi.org/10.1109/JSAC.2024.3389126

Gong TR, Gavriilidis P, Ji R, et al., 2024b. Holographic MIMO communications: theoretical foundations, enabling technologies, and future directions. *IEEE Commun Surv Tutor*, 26(1):196-257. https://doi.org/10.1109/COMST.2023.3309529

Govindarajan H, Pavone SC, Di Donato L, et al., 2020. Design of a compact dual circular-polarized antenna for L-band satellite applications. *IEEE Antenn Wirel Propag Lett*, 19(4):547-551. https://doi.org/10.1109/LAWP.2020.2971322

Hossen MS, Hoque A, Islam MT, et al., 2024. DNG metamaterial-inspired slotted stub antenna with enhanced gain, efficiency, and distributed current for early stage bone fracture detection applications. *IEEE Sens J*, 24(22):37932-37946. https://doi.org/10.1109/JSEN.2024.3459794

Lee S, Yoon D, Hwang K, et al., 2025. Wideband fan-beam lens antenna for IR-UWB through-the-wall human detection radar. *IEEE Sens J*, 25(7):11246-11257. https://doi.org/10.1109/JSEN.2025.3543804

Li H, Xiong Y, Zhang BX, et al., 2025. Simulation of precipitation echoes from airborne dual-polarization weather radar based on a fast algorithm for invariant imbedding T-matrix. *IEEE Trans Radar Syst*, 3:135-154. https://doi.org/10.1109/TRS.2024.3516745

Liu HP, Zhang YH, Zhao XW, 2024. A wideband circularly polarized antenna array loaded with dual-layer metasurface. *IEEE Trans Antenn Propag*, 72(8):6717-6722. https://doi.org/10.1109/TAP.2024.3365269

Mao Y, Huang Y, Yu XT, et al., 2024. Radio frequency interference mitigation in SAR systems via multi-polarization framework. *IEEE Trans Geosci Remote Sens*, 62:5210216. https://doi.org/10.1109/TGRS.2024.3384953

Moharana M, Dwivedy B, 2024. Circularly polarized planar antennas with enhanced characteristics for contemporary wireless communication use cases: a review. *IEEE Access*, 12:134594-134613. https://doi.org/10.1109/ACCESS.2024.3415483

Nekrasov A, Dell'Acqua F, 2016. Airborne weather radar: a theoretical approach for water-surface backscattering and wind measurements. *IEEE Geosci Remote Sens Mag*, 4(4):38-50. https://doi.org/10.1109/MGRS.2016.2613840

Notaroš BM, 2022. Polarimetric weather radar: overview of principles and applications. *IEEE Antenn Propag Mag*, 64(5):43-54. https://doi.org/10.1109/MAP.2022.3143442

Ogawa K, Tsagaanbayar D, Nakamura R, 2024. ISAR imaging for drone detection based on backprojection algorithm using millimeter-wave fast chirp modulation MIMO radar. *IEICE Commun Expr*, 13(7):276-279. https://doi.org/10.23919/comex.2024XBL0054

Reddy MH, Sheela D, 2023. A high gain dual circularly polarized X-band antenna for CubeSat applications. *Microw Opt Technol Lett*, 65(3):852-858. https://doi.org/10.1002/mop.33557

Schlaffer S, Schlögl M, 2024. Snow avalanche debris analysis using time series of dual-polarimetric synthetic aperture radar data. *IEEE J Sel Top Appl Earth Obs Remote Sens*, 17:12567-12578. https://doi.org/10.1109/JSTARS.2024.3423403

Sharif A, Kumar R, Althobaiti T, et al., 2023. Bio-inspired circular-polarized UHF RFID tag design using characteristic mode analysis. *IEEE Sens J*, 23(10):10847-10855. https://doi.org/10.1109/JSEN.2023.3262323

Shen YZ, Zhou SG, Huang GL, et al., 2016. A compact dual circularly polarized microstrip patch array with interlaced sequentially rotated feed. *IEEE Trans Antenn Propag*, 64(11):4933-4936. https://doi.org/10.1109/TAP.2016.2600747

Shi TY, Mao XH, Jakobsson A, et al., 2022. Extended PGA for spotlight SAR-filtered backprojection imagery. *IEEE Geosci Remote Sens Lett*, 19:4516005. https://doi.org/10.1109/LGRS.2022.3223164

Shokr ME, 1998. Field observations and model calculations of dielectric properties of Arctic sea ice in the microwave C-band. *IEEE Trans Geosci Remote Sens*, 36(2):463-478. https://doi.org/10.1109/36.662730

Sun MJ, Liu NW, Zhu L, et al., 2020. Wideband circularly polarized sequentially rotated microstrip antenna array with sequential-phase feeding network. *J Commun Inform Netw*, 5(3):350-357. https://doi.org/10.23919/JCIN.2020.9200898

Ta SX, Nguyen VC, Nguyen-Thi BT, et al., 2022. Wideband dual-circularly polarized antennas using aperture-coupled stacked patches and single-section hybrid coupler. *IEEE Access*, 10:21883-21891. https://doi.org/10.1109/ACCESS.2022.3155120

Wang XF, Guo LY, Zhou WQ, et al., 2024. A double-layer multimode metasurface antenna using characteristic mode analysis. *IEEE Antenn Wirel Propag Lett*, 23(10):3237-3241. https://doi.org/10.1109/LAWP.2024.3433005

Weber M, Hondl K, Yussouf N, et al., 2021. Towards the next generation operational meteorological radar. *Bull Amer Meteorol Soc*, 102(7):E1357-E1383. https://doi.org/10.1175/BAMS-D-20-0067.1

Xie JB, Wen JJ, Chen JW, et al., 2022. Microwave icing sensor based on interdigital-complementary split-ring resonator. *IEEE Sens J*, 22(13):12829-12837. https://doi.org/10.1109/JSEN.2022.3176932

Xie JB, Li ZH, Lu BS, et al., 2024. A flexible CSRR-based array icing sensor with defective microstrip structure. *IEEE Sens J*, 24(12):19934-19943. https://doi.org/10.1109/JSEN.2024.3395435

Xu R, Gao SS, Liu J, et al., 2020. Analysis and design of ultrawideband circularly polarized antenna and array. *IEEE Trans Antenn Propag*, 68(12):7842-7853. https://doi.org/10.1109/TAP.2020.2998922

Yin JP, Chen HN, Li YZ, et al., 2021. Clutter mitigation based on spectral depolarization ratio for dual-polarization weather radars. *IEEE J Sel Top Appl Earth Obs Remote Sens*, 14:6131-6145. https://doi.org/10.1109/JSTARS.2021.3088324

Zhang JJ, Jin ZF, Song YF, et al., 2024. Back-projection operator-based one-stationary bistatic SAR sparse imaging. *IEEE Geosci Remote Sens Lett*, 21:4012405. https://doi.org/10.1109/LGRS.2024.3416518

Zhang L, Zou Q, Chu HB, et al., 2024. A multifunctional magneto-electric dipole antenna with pattern and polarized reconfigurability. *IEEE Antenn Wirel Propag Lett*, 23(8):2396-2400. https://doi.org/10.1109/LAWP.2024.3393108

Zhao C, Wang CF, 2018. Characteristic mode design of wide band circularly polarized patch antenna consisting of H-shaped unit cells. *IEEE Access*, 6:25292-25299. https://doi.org/10.1109/ACCESS.2018.2828878

Zhao XQ, Lian RN, Qin M, et al., 2024. A high-gain Fabry–Perot resonator antenna with dual-sense circular polarization diversity. *IEEE Antenn Wirel Propag Lett*, 23(12):4029-4033. https://doi.org/10.1109/LAWP.2024.3403803